



HAL
open science

Wireless Enhanced Electrochemiluminescence at a Bipolar Microelectrode in a Solid-State Micropore

Silvia Voci, Abdulghani Ismail, Pascale Pham, Jing Yu, Ali Maziz, Fabien Mesnilgrente, Lucile Reynaud, Thierry Livache, Pascal Mailley, Arnaud Buhot, et al.

► **To cite this version:**

Silvia Voci, Abdulghani Ismail, Pascale Pham, Jing Yu, Ali Maziz, et al.. Wireless Enhanced Electrochemiluminescence at a Bipolar Microelectrode in a Solid-State Micropore. *Journal of The Electrochemical Society*, 2020, 167 (13), pp.137509. 10.1149/1945-7111/abbbc1 . hal-03024426

HAL Id: hal-03024426

<https://laas.hal.science/hal-03024426>

Submitted on 25 Nov 2020

HAL is a multi-disciplinary open access archive for the deposit and dissemination of scientific research documents, whether they are published or not. The documents may come from teaching and research institutions in France or abroad, or from public or private research centers.

L'archive ouverte pluridisciplinaire **HAL**, est destinée au dépôt et à la diffusion de documents scientifiques de niveau recherche, publiés ou non, émanant des établissements d'enseignement et de recherche français ou étrangers, des laboratoires publics ou privés.

OPEN ACCESS

Wireless Enhanced Electrochemiluminescence at a Bipolar Microelectrode in a Solid-State Micropore

To cite this article: Silvia Voci *et al* 2020 *J. Electrochem. Soc.* **167** 137509

View the [article online](#) for updates and enhancements.

239th ECS Meeting

with the 18th International Meeting on Chemical Sensors (IMCS)

ABSTRACT DEADLINE: DECEMBER 4, 2020



May 30-June 3, 2021

SUBMIT NOW →



Wireless Enhanced Electrochemiluminescence at a Bipolar Microelectrode in a Solid-State Micropore

Silvia Voci,^{1,=} Abdulghani Ismail,^{2,=} Pascale Pham,³ Jing Yu,¹ Ali Maziz,⁴ Fabien Mesnilgrete,⁴ Lucile Reynaud,² Thierry Livache,² Pascal Mailley,³ Arnaud Buhot,² Thierry Leichle,^{4,5} Alexander Kuhn,¹ Loic Leroy,² Aurélie Bouchet-Spinelli,^{2,z} and Neso Sojic^{1,z}

¹Univ. Bordeaux, Bordeaux INP, ISM, UMR CNRS 5255, 33607 Pessac, France

²Univ. Grenoble Alpes, CEA, CNRS, IRIG, SYMMES, F-38000 Grenoble, France

³Univ. Grenoble Alpes, CEA LETI, F-38000, Grenoble, France

⁴LAAS-CNRS, Université de Toulouse, 31400 Toulouse, France

⁵Georgia Tech-CNRS Joint International Laboratory, School of Electrical and Computer Engineering, Atlanta, GA, United States of America

The combination of bipolar electrochemistry (BE), as a wireless electrochemical approach, and of electrochemiluminescence (ECL) as an imaging readout is a successful strategy with a wide range of analytical applications. However, small conductive entities such as micrometric and nanometric objects are particularly difficult to polarize by BE since they require extremely high electric fields. In order to circumvent this issue due to intrinsic limitations of BE, we elaborated a solid-state micropore, decorated with a rhombus-shaped gold microelectrode. The electric field strength was concentrated inside the solid-state micropore where the conductive gold microelectrode was precisely located and acted as a bipolar light-emitting device. This original configuration allowed achieving adequate polarization of the gold microelectrode in a wireless manner, which led locally to ECL emission. ECL imaging shows that light was generated by the bipolar microelectrode in the center of the micropore. ECL emission could be achieved by imposing a potential value (10 V) to the feeder electrodes that is more than 2 orders of magnitude lower than those required without the micropore. The reported ECL approach opens exciting perspectives for the development of original wireless bioanalytical applications and dynamic bipolar experiments with small objects passing through the pores.

© 2020 The Author(s). Published on behalf of The Electrochemical Society by IOP Publishing Limited. This is an open access article distributed under the terms of the Creative Commons Attribution 4.0 License (CC BY, <http://creativecommons.org/licenses/by/4.0/>), which permits unrestricted reuse of the work in any medium, provided the original work is properly cited. [DOI: 10.1149/1945-7111/abbcb1]



Manuscript submitted August 9, 2020; revised manuscript received September 24, 2020. Published October 7, 2020. *This paper is part of the JES Focus Issue on IMCS 2020.*

Supplementary material for this article is available [online](#)

Electrochemiluminescence (ECL) is a sensitive analytical technique, which is widely applied in analytical chemistry for the detection of clinical biomarkers, biological warfare agents and foodborne pathogens, as well as for microscopy of cells, micro/nanoparticles and electrochemical processes.^{1–4} The light emission results from an initial electrochemical step. It involves a light-emitting species, the luminophore, and a sacrificial coreactant species, whose role is to provide highly energetic radicals upon electrochemical reactions. ECL starts with a heterogeneous electron-transfer reaction at the electrode surface, continues with a cascade of homogeneous reactions with a coreactant species, which produces the excited state of a luminophore, and ends with photon emission. Most of the analytical applications in aqueous media rely on the use of ruthenium(II) tris(bipyridine), [Ru(bpy)₃]²⁺, and tri-*n*-propylamine (TPA) as the luminophore and the coreactant, respectively.^{5,6} This tandem model system is highly efficient and generates bright emission. In ECL, the analytical information is contained in the light signal and its intensity is directly proportional to the concentration of a limiting reactant (typically, the luminophore or the coreactant) involved in the ECL process. ECL combines thus intimately the initial electrochemical stimulation and the final optical signal. ECL has been used to image various electrochemical processes,^{7–9} surfaces^{10–12} or objects^{13,14} as well as cells.^{15–21} ECL was also investigated in various confined configurations.^{7,10,11,22–24}

In the last decade, ECL was successfully combined with bipolar electrochemistry (BE) because it is a wireless electrochemical technique.^{25–33} Indeed, due to this contactless nature, classical BE setups do not allow to measure directly an electrochemical signal reflecting the reactivity of the investigated conductive object in a

straightforward way. In BE, the electrochemical addressing of conducting objects is achieved without physical connection to a power supply through an electric contact.^{34–36} In the most common “open” configuration, two feeder electrodes are connected to a power supply and immersed in an ionically conducting media. An electronically-conducting object is positioned in solution in the electric field generated by both feeder electrodes. In a first order approximation, the electric field can be considered as a linear potential drop across the solution. As the conductive object is by definition at an equipotential value, an interfacial polarization potential is established alongside the object.^{37,38} When the potential drop and thus the resulting polarization potential is high enough, the object acts as a bipolar electrode with cathodic and anodic features at its two extremities. This triggers simultaneously reduction and oxidation reactions at its surface with the cathodic and anodic poles facing the feeder anode and cathode, respectively. In other words, different electrochemical processes occur concomitantly at the surface of the bipolar object. Thanks to its intrinsic features (i.e. wireless, duality of the redox reactions, gradients of electrochemical reactivity), BE has attracted in the last few years an exponentially increasing interest in different fields.^{39–44} Since ECL combines electrochemical addressing and orthogonal optical readout, it complements very efficiently with BE. Indeed, the optical output of ECL may reflect the electrochemical reactivity of the bipolar objects in different configurations as initially demonstrated by Manz and Crooks.^{25,45} The combination of ECL and BE has been successfully applied mainly in analytical chemistry, for the measurement of different biomolecules using various detection strategies, as well as for the development of dynamic ECL “swimmers”.^{31,46–50} However, addressing micrometric or nanometric objects by BE remains a difficult task, because it requires high electric fields. Indeed, the shorter the conducting object (more precisely, the effective length along the axis parallel to the electric field vector), the larger is the

⁼These authors contributed equally to this work.

^zE-mail: Aurelie.Bouchet-Spinelli@cea.fr; Neso.Sojic@enscbp.fr

electric field required to polarize it in order to induce both electrochemical reactions at its poles.³⁴ Therefore, this drawback for polarizing small objects due to the inherent physical features of BE represents a challenging issue which needs to be overcome.⁵¹

One of the main factors governing BE is the potential drop across the solution.³⁴ Therefore, shaping the spatial distribution of the potential drop may open new perspectives for BE. The spatial confinement of this potential drop has been achieved using micropore and nanopore technology.^{52–55} Indeed, a sharp potential drop can be generated at the level of such spatial restrictions. Modified nanopipettes have been used to detect various analytes by BE or ECL.^{52,56–58} For example, Long et al. described the detection of NADH in living cells using an asymmetric nanopore electrode with a diameter down to 90 nm.⁵⁶ The potential drop was focused at the nanopore electrode, which converts the faradaic current into a bubble-induced transient ionic current. Zhang et al. reported the measurement of single nanoparticles passing through a bipolar nanopore.^{40,59} Jiang et al. modified the internal walls of a nanopipette tip with Pt to perform wireless ECL analysis of single living cells.⁶⁰ Recently, we reported solid-state micropores for bipolar ECL.⁶¹ We used a deoxidized silicon 20- μm long path to demonstrate its wireless polarization and ECL emission.

Herein, we extend this approach based on solid-state planar micropores⁶¹ by integrating a rhombus-shaped (dimensions: $6 \times 3 \mu\text{m}$) Au microelectrode in a microfluidic channel (Fig. 1). The goal was to demonstrate the possibility to address a single conductive object located in the micropore. A Au microelectrode was precisely fabricated in the middle of the micropore, in the region where the highest potential drop occurs. ECL was generated using the model $[\text{Ru}(\text{bpy})_3]^{2+}/\text{TPA}$ system at very low potentials considering the effective length of the rhombus-shaped Au microelectrode along the axis of the electric field vector (i.e. $3 \mu\text{m}$). Oxidation of the ECL reagents at the anodic pole of the bipolar electrode leads to strong ECL signals. ECL imaging shows that emission occurs in the middle of the micropore at the level of the bipolar Au microelectrode. The fabricated device comprises two features: (i) a spatial restriction,

which focuses the potential drop (ii) a bipolar microelectrode that emits ECL light in a wireless manner. Using this set-up, we were able to polarize a microelectrode, which is almost 7-times shorter than the length of the micropore, with a very low potential difference (10 V). Finally, the localized potential drop was rationalized by finite element simulations.

Experimental

Chemicals.—All chemicals were obtained from Sigma-Aldrich except SU-8 2075, which was purchased from Microchem. Tris (2,2'-bipyridyl)dichlororuthenium(II) hexahydrate and tri-*n*-propylamine were prepared in phosphate buffer solution (0.1 M, pH 7.4). The conductivity of the solution was 13.9 mS cm^{-1} .

Fabrication of silicon microchips with an integrated micropore.—The micropore chips were fabricated using top-down micro-machining (Fig. 2) onto 100 mm *n*-type silicon substrates ($\rho < 0.01 \Omega \text{ cm}$) cleaned by oxygen plasma in a Diener machine (800 W, 5 min) prior processing. The micropore patterns were transferred onto the silicon wafers by a photolithography step followed by reactive ion etching for a total depth of $20 \mu\text{m}$. Photolithography was performed with spin-coated positive photoresist ECI 3012 $2.5 \mu\text{m}$ and the micropatterns were etched in the silicon using SF_6 (250 sccm), C_4F_8 (250 sccm), and O_2 (35 sccm). The plasma source was generated by an inductively coupled plasma source manufactured by Alcatel Comptech Inc. The residual photoresist layer was removed by acetone and O_2 plasma (800 W, 5 min). Then, dry thermal oxidation was performed in a furnace to grow 300 nm of SiO_2 onto the silicon wafers. Finally, metal electrodes were patterned on the SiO_2 layer by photolithography and wet etching. Briefly, a layer of Ti/Au of 50 nm/200 nm was first deposited by physical vapor deposition using a Univex 450 C and etched in appropriate baths after carrying out photolithography with the positive photoresist AZ 4999. The wafers were finally diced into $20 \text{ mm} \times 20 \text{ mm}$ chips, each one containing a single micropore.

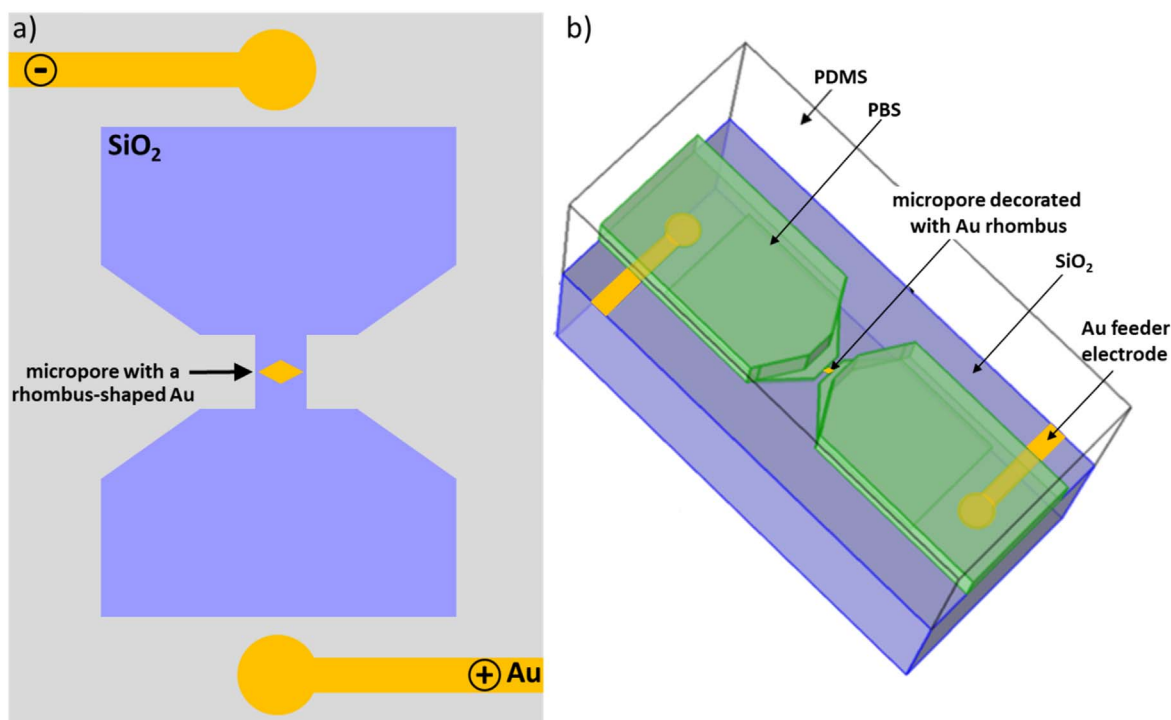


Figure 1. Schematic representations of the silicon microchip integrating the solid-state micropore, which was decorated with a rhombus-shaped bipolar Au electrode (yellow color). Top view (a): The Au feeder electrodes (yellow color) are shown. 3D view (b): the silicon microchip was covered with a PDMS mold (transparent color) that was specifically designed in order to define a microfluidic channel filled with the PBS solution (green color) and the ECL reagents. The top view scheme (a) is not to scale, the 3D view (b) is to scale.

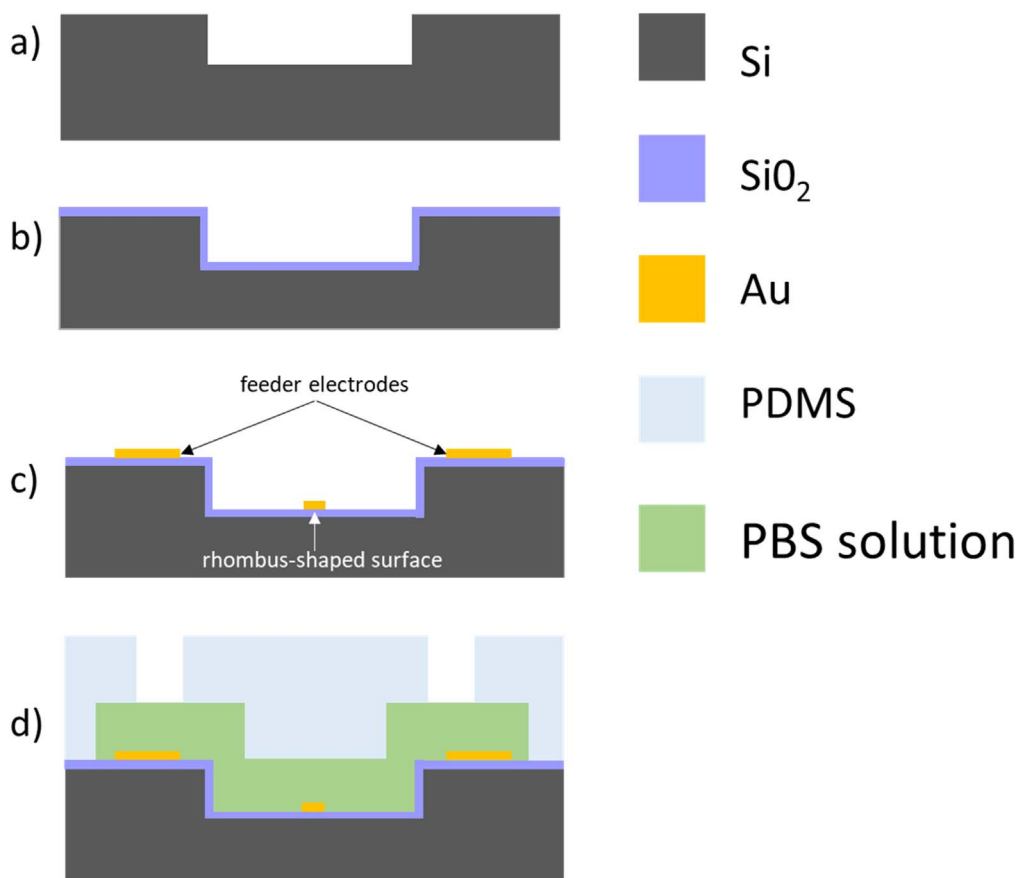


Figure 2. Fabrication process flow of the silicon microchip. Cross section view along the middle of the micropore. (a) Micropore fabrication on the silicon wafer by photolithography followed by reactive ion etching. (b) Dry thermal oxidation of the silicon wafer to grow 300 nm of SiO₂. (c) Patterning of feeder Au electrodes and the rhombus-shaped Au surface by photolithography and wet etching techniques. (d) Encapsulation of the microfluidic channel in a molded PDMS slab and filling the fluidic channel with PBS solution. The scheme is not to scale.

SU-8 on silicon mold was fabricated by a conventional photolithography process in order to prepare the PDMS channels (Fig. 1b). Briefly, a 4-inch silicon wafer was sonicated for 5 min in acetone then in isopropanol (IPA). It was then dried at 180 °C for 15 min and SU-8 2075 negative photoresist was spin coated for 5 s at 500 rpm followed by 30 s at 2000 rpm then another 5 s at 500 rpm. The acceleration was always 300 rpm s⁻¹. Following this, soft baking at 65 °C for 5 min then 95 °C for 20 min, and finally 65 °C for 5 min was applied. The design of the channels was drawn using KLayout. It was directly written on the resist via laser photolithography (70 mW, 70%) (μ PG 101 Heidelberg Instrument, Germany) followed by a post exposure bake (PEB) at 65 °C for 2 min then 95 °C for 8 min. The unexposed parts of the resist were removed by developing in SU-8 developer for 10 min then in IPA for 30 s. In order to make the SU-8 motifs very resistant, a hard bake at 150 °C for 15 min was carried out. The height of the channel (140 μ m) was characterized with a profilometer (Dektak DXT “E”, USA).

The chips were finally capped with a PDMS microfluidic channel⁶² by pouring a mixture of elastomer and curing agent at a ratio of 10/1 onto the SU-8 mold after proper degassing. The PDMS was cured at 60 °C for 1 h before demolding. The prepared PDMS and the silicon chips were activated using oxygen plasma and they were aligned using a MJB4 mask aligner from Suss MicroTec before bringing them together.

Instrumentation.—Voltammetric and ECL experiments were performed with a PGSTAT30 Autolab potentiostat connected to a conventional three-electrode cell. ECL intensity was measured using a Hamamatsu photomultiplier tube (PMT) R5070A with a Hamamatsu C9525 high voltage power supply. The output signal

was amplified by a Keithley 6485 Picoammeter before acquisition via the second input channel of the PGSTAT30 Autolab potentiostat.

Potential pulses of 10 V with a duration of 300 ms and separated by a delay of 100 ms were applied for 10 s using a DG1032 power supply from Rigol. ECL images were recorded using an epifluorescence Leica (DMI6000, Leica Microsystems) microscope equipped with an EM-CCD 9100-13 camera from Hamamatsu. All experiments were performed at ambient temperature (25 °C). Exposure time of the CCD camera was synchronized with the potential application for 10 s. The images were treated using Image J software.

SEM images were obtained with a FEI Helios 600i SEM instruments.

Finite element simulation.—To study the electrochemical behavior of the micropore with an integrated bipolar microelectrode, finite element simulations were performed using the Finite Element code Comsol Multiphysics™, by solving Maxwell’s equations using the Static and Low-Frequency Electromagnetics module (ACDC).⁶³ A simplifying assumption of this numerical model was to consider that no electrochemical double layer was formed at the feeder electrodes surface. The potential applied to the Au feeder electrodes was -5 and +5 V respectively. The electrical conductivity of the saline solution was measured (13.9 mS cm⁻¹). The description of the finite element model is detailed in the Supporting Information.

Results and Discussion

Fabrication of the microfluidic device with the micropore and the rhombus-shaped Au surface.—We designed a microfluidic device comprising the following main components: a planar solid-

state micropore, a single rhombus-shaped Au microelectrode (without physical connection) and two feeder Au electrodes. These spatial restrictions are considered as planar because they are at the surface of the substrate and not drilled through the silicon chips. The devices were fabricated on 100 mm n-type silicon substrates using standard micromachining techniques (Fig. 2). Details of the fabrication process of the solid-state micropore itself have been described previously.⁶¹ However, we modified the fabrication steps to integrate the rhombus-shaped Au surface in the devices (Fig. 2). In the present work, we added a rhombus-shaped Au microelectrode in the micropore structure. Briefly, photolithography was first used to pattern the micropores, consisting of rectangular cavities with a constriction that was subsequently transferred to the silicon wafer by reactive ion etching (for a total depth of 20 μm). The SEM images of the devices were recorded at different magnifications (Fig. 3). They show the dimensions of the micropore: 20 μm length, 10 μm width and 20 μm height. After, removing the residual photoresist layer by acetone and plasma O_2 , dry thermal oxidation was performed in a furnace to grow 300 nm of an insulating SiO_2 layer. This layer is thick enough to prevent any electrochemical reactions between the silicon substrate and the ECL reagents dissolved in solution. The Au feeder electrodes and rhombus-shaped gold features were fabricated by first depositing sequentially 50 nm/200 nm Ti/Au layers by physical vapor deposition on the oxidized silicon and patterning the layers by photolithography and wet etching. The wafers were then diced into 20 mm \times 20 mm chips containing a single micropore. The two Au feeder electrodes with a radius of 50 μm were fabricated at the extremities of the chip. The center-to-center distance d between them was 1.2 mm. The lengths of the short and long diagonals of the rhombus-shaped Au microelectrode were $6 \times 3 \mu\text{m}$, respectively. The chips were finally capped with a PDMS microfluidic channel created by pouring a mixture of elastomer and curing agent (Figs. 1b and 2). Since the PDMS is a transparent material in the visible range, it allowed light transmission during ECL imaging experiments. These fabrication steps lead to a microfluidic device with a solid-state micropore, which integrates a rhombus-shaped Au bipolar microelectrode.

Bipolar electrochemical properties.—To generate ECL in the bipolar configuration, it is necessary to estimate the potential required to oxidize the ECL reagents as well as the potential of the reduction reaction. The latter one has to counter-balance the charge resulting from the reaction on the other pole of the bipolar electrode. Indeed, the rate of the oxidation reaction has to be equal to the reduction process due to global charge neutrality at the level of the bipolar electrode. The polarization ΔV_{BE} required to generate both faradaic reactions at the Au surface was estimated by recording the linear voltammetric signals at a conventional Au working

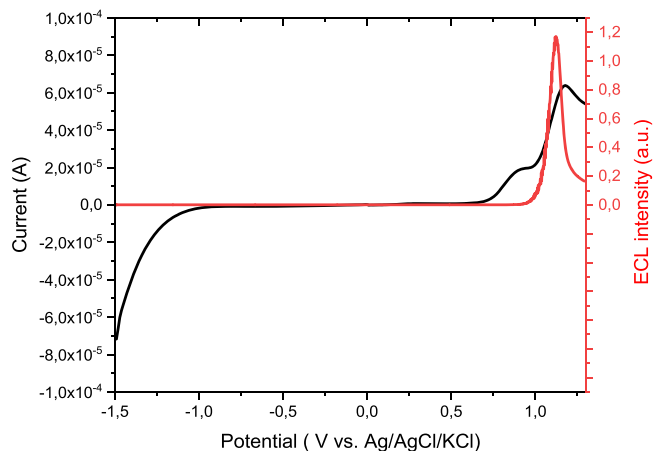


Figure 4. Linear voltammogram (black curve) and ECL signal (red curve) of 1 mM $[\text{Ru}(\text{bpy})_3]^{2+}$ in the presence of 50 mM TPA in PBS (pH 7.4) recorded on an Au working electrode at a scan rate of 0.1 V s^{-1} in a classic 3-electrode setup.

electrode (Fig. 4, black curve). This electrochemical experiment has been combined with a simultaneous monitoring of the ECL intensity (Fig. 4, red curve). ECL intensity starts to increase significantly at +1 V vs Ag/AgCl/KCl before decreasing rapidly above 1.1 V vs Ag/AgCl/KCl. This decrease is due to the surface oxide formation on Au in aqueous media, which prevents the efficient oxidation of the amine-based coreactant. The cathodic current (black curve), which corresponds to the reduction of dioxygen and water increases for potential values below -1 V vs Ag/AgCl/KCl. Considering the value of the anodic current at the potential required to generate ECL, a potential of approximately -1.5 V vs Ag/AgCl/KCl is necessary to obtain a cathodic current of the same intensity. Therefore, a minimal polarization potential difference ΔV_{BE} of 2.6 V is required for coupling both reactions on a Au surface in the bipolar configuration.

In a classical BE configuration, the polarization potential ΔV_{BE} induced on a conducting object is proportional to the external electric field ($\Delta V_{FE}/d$) and the effective length l of the object along the axis aligned to the electric field vector, as described by the simple equation:

$$\Delta V_{BE} = \frac{\Delta V_{FE}}{d} \cdot l \quad [1]$$

with ΔV_{FE} being the potential difference applied between the two feeder electrodes.

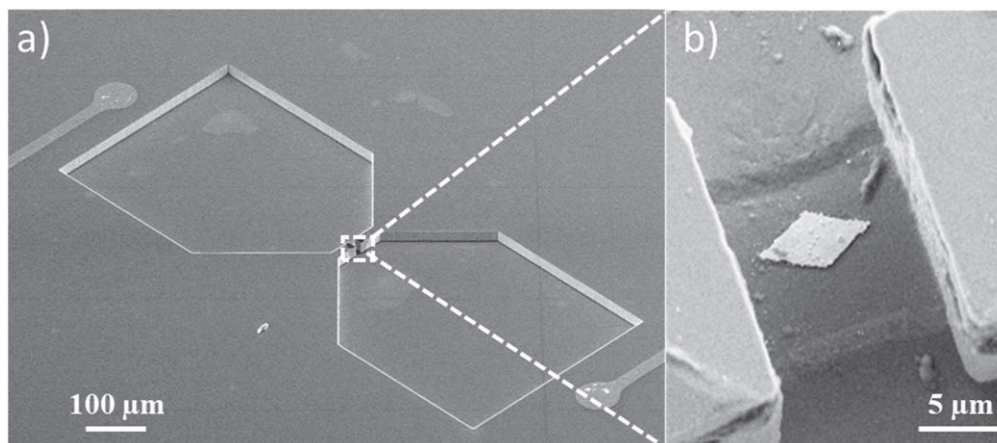


Figure 3. (a) SEM image of the microchip with the micropore ($10 \times 10 \times 20 \mu\text{m}$) and the integrated feeder Au electrodes. (b) Zoom on the ECL-emitting rhombus-shaped Au surface ($6 \times 3 \mu\text{m}$) positioned at the bottom surface of the micropore.

This equation is a first order approximation, which does not take into account potential drops at the feeder electrodes due to the electrochemical double layer. Considering that ΔV_{BE} and l are 2.6 V and 3 μm , respectively, Eq. 1 states that the electric field has to be at least *ca.* 8.7 kV cm^{-1} . In the present chip with $d = 1.2$ mm, it would correspond to a potential ΔV_{FE} of 1040 V. This value is coherent with a difference potential ΔV_{FE} of 30 kV imposed in classical BE ($d = 45$ cm) to modify 2 μm long carbon nanotubes with Au deposits ($\Delta V_{BE} = 0.24$ V).⁵¹ In brief, ECL emission was achieved at the rhombus-shaped bipolar microelectrode by imposing a potential difference of only 10 V to the feeder electrodes (*vide infra*). This value is more than 2 orders of magnitude lower than potentials required without the micropore structure.

ECL imaging of the rhombus-shaped bipolar microelectrode.—

The ECL mechanism of the model $[\text{Ru}(\text{bpy})_3]^{2+}/\text{TPA}$ system is an active area of investigation with several competitive pathways,^{64,65} which depends on several experimental parameters (e.g. electrode material, surface hydrophobicity, concentration ratio, pH value, etc.).⁶⁶ In the present case, the mechanism involves oxidation of both ECL reagents, which then react together to produce the excited state, $[\text{Ru}(\text{bpy})_3]^{2+*}$, and thus, ECL emission. As already mentioned, the passivation of the electrode surface by the growth of an oxide layer at the potentials required for ECL generation may decrease the ECL signal by preventing the efficient TPA oxidation. To avoid this effect, we pulsed rapidly the potential ΔV_{FE} of the feeder electrodes from 0 to 10 V for 300 ms with a rest potential of 0 V for 100 ms. Using lower potential values makes it impossible to record ECL images at the level of the bipolar Au microelectrode. A higher potential leads to unstable ECL signals. In other words, thanks to the micropore, a potential of 10 V is a good compromise to produce efficiently ECL at the rhombus-shaped Au surface without passivating it. Since silicon is an opaque substrate, which does not allow light transmission, the photoluminescent (PL) and ECL images have been recorded from the top through the PDMS layer. Figure 5a displays the PL image of the micropore without imposing any external potential to the feeder electrodes. It shows that the micropore and the microfluidic device were filled with the solution containing the PL-active $[\text{Ru}(\text{bpy})_3]^{2+}$ luminophore (and the co-reactant). The excitation light was then turned off and the potential pulses were applied. Figures 5b–5c reveal that ECL emission is confined in the middle of the micropore where the rhombus-shaped Au surface is located. The ECL image shows a bright spot of light with a disk pattern. From the ECL images, we extracted the ECL intensity profiles along both normal axes passing by the short (blue curve) and long (black curve) diagonals of the microfabricated

rhombus Au surface. The short axis of the rhombus is parallel to the longitudinal axis of the micropore whereas its long axis is perpendicular to it (Fig. 3). Both curves overlay. The full-width at half-maximum for both ECL intensity profiles is ~ 8 μm whereas the dimensions of the rhombus were 6 $\mu\text{m} \times 3$ μm . In fact, the ECL-emitting region should be even smaller than half of the rhombus-shaped Au surface because reduction of dioxygen and water occurs simultaneously on the cathodic pole of this bipolar element. The fact that we were not able to resolve better the size and the shape of the rhombus surface by ECL imaging is most probably due to the low optical resolution resulting from the transmission through the 2.5-millimeter thick PDMS layer covering the microchip. In previous works,^{22,23} we investigated also ECL in confined environments. The ECL patterns were different because light was generated either in the nanochannel at or the level of the access hole areas depending on the annihilation or coreactant modes, respectively.

To generate ECL, a potential ΔV_{FE} of 10 V was imposed at the feeder electrodes. This experimental value is much smaller than the 1040 V value calculated theoretically using Eq. 1 and which is required for a configuration without the micropore structure. This imposed potential, which is more than 2 orders of magnitude lower than the theoretically predicted one in a classic bipolar configuration, is due to the sharp potential drop focused at the level of the micropore. Indeed, this spatial restriction leads to enhanced local polarization and ECL emission. Finite element simulations were performed to study the distribution of the polarization at the level of the bipolar Au microelectrode in the micropore.

Finite element simulations.—

As mentioned previously, the spatial distribution of the potential is the pertinent experimental parameter, which determines the electrochemical reactions, their rates and their locations at the level of the bipolar electrode. Figure 6a shows the electric potential distribution calculated by finite element simulations without taking into account the effects of the electrochemical double layer. It shows that the potential drop is mostly confined inside the micropore where the bipolar Au rhombus microelectrode is positioned. This feature allows polarizing it and generating ECL at low potential values applied to the feeder electrodes. We calculated also the norm of the electric field along the axis passing through the short diagonals of the rhombus (Fig. 6b). This simulated profile shows that the highest values of the electric field are located at the extremities of the Au electrode (of the order of MV m^{-1}), confirming that the gold layer in the pore acts as a bipolar electrode.

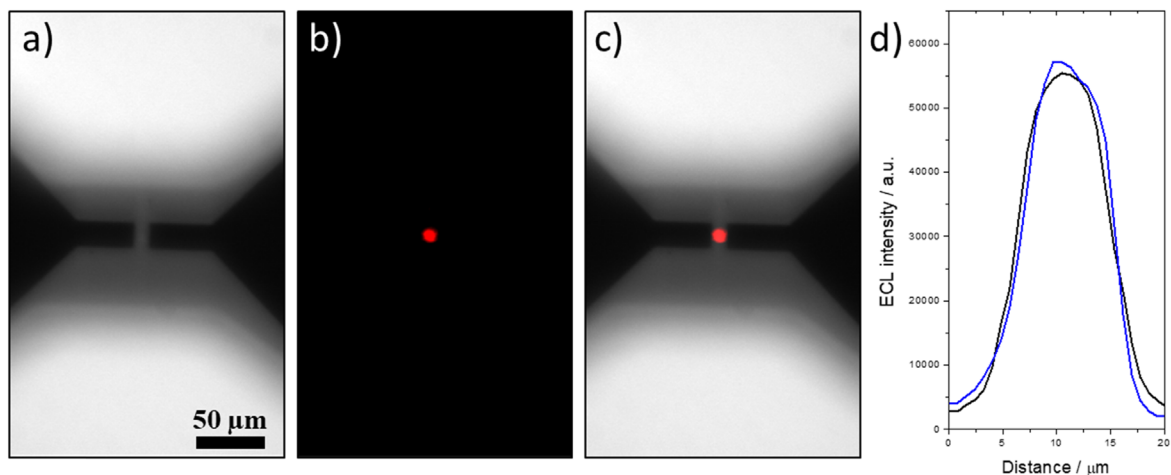


Figure 5. (a) PL, (b) ECL and (c) overlaid images of the ECL-emitting bipolar Au microelectrode confined in the micropore. The rhombus-shaped Au surface was polarized remotely by the feeder electrodes. The ECL image was recorded in PBS (pH 7.4) containing 1 mM $[\text{Ru}(\text{bpy})_3]^{2+}$ and 50 mM TPA by applying a sequence of 10 potential pulses of 10 V for 0.3 s, followed by 0 V for 0.1 s, respectively. (d) ECL intensity profiles along both normal axes along the short (blue curve) and the long (black curve) diagonals of the rhombus.

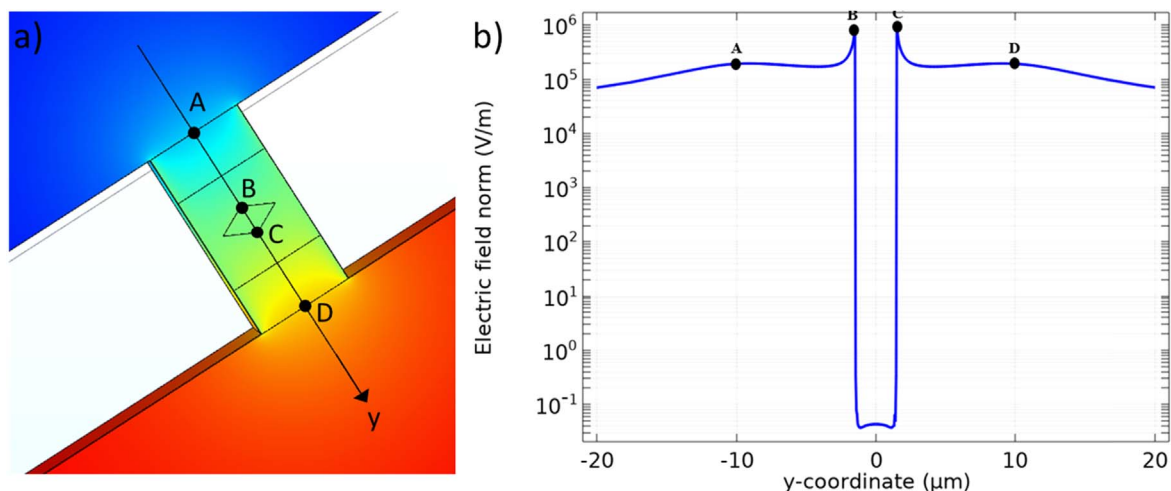


Figure 6. Finite element simulation results (0 Hz): (a) electric potential distribution in the vicinity of the micropore, (b) profile of the norm of the electric field along the y-axis passing by the short diagonals of the rhombus (i.e. along the middle of the micropore through the Au rhombus layer; A-B-C-D points showed on Fig. 6a). The image was coded according to a color scale of the potential where red and blue colors represent +5 V and -5 V, respectively.

Conclusions

In summary, an analytical fluidic device comprising a solid-state micropore decorated with a rhombus-shaped Au microelectrode was designed and fabricated. The potential drop was confined at the level of the micropore where a microelectrode was precisely positioned. This configuration allowed polarizing remotely the rhombus-shaped Au microelectrode at very low potentials. Indeed, thanks to the micropore features, only a potential difference of 10 V needs to be imposed between the feeder electrodes to generate ECL, instead of the 100-fold higher potential theoretically required in a configuration without the micropore. The electrochemical addressing was revealed using ECL emission of the model $[\text{Ru}(\text{bpy})_3]^{2+}/\text{TPA}$ system. Strong ECL light was emitted in the middle of the micropore by the Au microelectrode, demonstrating the wireless polarization. The unique micropore properties were rationalized by finite element simulations, which showed the electric field distribution. The reported strategy could be extended to elaborate a variety of bipolar ECL devices with interesting high-throughput features with parallelized micropores. Finally, it paves the way to dynamic bipolar experiments for the ECL detection of micro/nano-objects passing through the pores, where they might generate ECL transiently during the translocation or modulate the ECL signal by hindering the diffusion of the ECL reagents.

Acknowledgments

We thank the Agence Nationale de la Recherche (Planpore ANR-15-CE18-0027). This work has been partially supported by Labex ARCANE and CBH-EUR-GS (ANR-17-EURE-0003). SyMMES laboratory is part of Labex LANEF program (ANR-10-LABX-51-01). This work has also been partially funded by the European Research Council (ERC) under the European Union's Horizon 2020 research and innovation program (grant agreement no 741251, ERC Advanced grant ELECTRA).

ORCID

Alexander Kuhn <https://orcid.org/0000-0002-1962-4863>
Aurélie Bouchet-Spinelli <https://orcid.org/0000-0003-1709-785X>
Neso Sojic <https://orcid.org/0000-0001-5144-1015>

References

- Z. Liu, W. Qi, and G. Xu, *Chem. Soc. Rev.*, **44**, 3117 (2015).
- M. Hesari and Z. Ding, *J. Electrochem. Soc.*, **163**, H3116 (2016).
- H. Qi and C. Zhang, *Anal. Chem.*, **92**, 524 (2020).
- P. Bertoncello and P. Ugo, *ChemElectroChem*, **4**, 1663 (2017).
- E. Kerr, E. H. Doeven, D. J. D. Wilson, C. F. Hogan, and P. S. Francis, *Analyst*, **141**, 62 (2016).
- Y. Yuan, S. Han, L. Hu, S. Parveen, and G. Xu, *Electrochim. Acta*, **82**, 484 (2012).
- C. Amatore, C. Pebay, L. Servant, N. Sojic, S. Szunerits, and L. Thouin, *ChemPhysChem*, **7**, 1322 (2006).
- C. M. Pharr, R. C. Engstrom, J. Klancke, and P. L. Unzelman, *Electroanalysis*, **2**, 217 (1990).
- J. Zhang, J. Zhou, C. Tian, S. Yang, D. Jiang, X.-X. Zhang, and H.-Y. Chen, *Anal. Chem.*, **89**, 11399 (2017).
- L. M. Moretto, T. Kohls, A. Chovin, N. Sojic, and P. Ugo, *Langmuir*, **24**, 6367 (2008).
- L. M. Moretto, T. Kohls, D. Badocco, P. Pastore, N. Sojic, and P. Ugo, *J. Electroanal. Chem.*, **640**, 35 (2010).
- C. J. Miller, P. McCord, and A. J. Bard, *Langmuir*, **7**, 2781 (1991).
- M.-J. Zhu, J.-B. Pan, Z.-Q. Wu, X.-Y. Gao, W. Zhao, X.-H. Xia, J.-J. Xu, and H.-Y. Chen, *Angew. Chem. Int. Ed.*, **57**, 4010 (2018).
- A. J. Wilson, K. Marchuk, and K. A. Willets, *Nano Lett.*, **15**, 6110 (2015).
- C. Cui, Y. Chen, D. Jiang, J.-J. Zhu, and H.-Y. Chen, *Anal. Chem.*, **89**, 2418 (2017).
- J. Xu, P. Huang, Y. Qin, D. Jiang, and H.-Y. Chen, *Anal. Chem.*, **88**, 4609 (2016).
- R. He, H. Tang, D. Jiang, and H.-Y. Chen, *Anal. Chem.*, **88**, 2006 (2016).
- G. Valenti et al., *J. Am. Chem. Soc.*, **139**, 16830 (2017).
- H. Ding, W. Guo, and B. Su, *Angew. Chem. Int. Ed.*, **59**, 449 (2020).
- H. Gao, W. Han, H. Qi, Q. Gao, and C. Zhang, *Anal. Chem.*, **92**, 8278 (2020).
- C. Ma, Y. Cao, X. Gou, and J.-J. Zhu, *Anal. Chem.*, **92**, 431 (2020).
- H. Al-Kutubi, S. Voci, L. Rassaei, N. Sojic, and K. Mathwig, *Chem. Sci.*, **9**, 8946 (2018).
- S. Voci, H. Al-Kutubi, L. Rassaei, K. Mathwig, and N. Sojic, *Anal. Bioanal. Chem.*, **412**, 4067 (2020).
- C. Ma, L. P. Z. Iii, and P. W. Bohn, *Chem. Sci.*, **6**, 3173 (2015).
- A. Arora, J. C. T. Eijkel, W. E. Morf, and A. Manz, *Anal. Chem.*, **73**, 3282 (2001).
- S. E. Fosdick, J. A. Crooks, B.-Y. Chang, and R. M. Crooks, *J. Am. Chem. Soc.*, **132**, 9226 (2010).
- W. Zhan, J. Alvarez, and R. M. Crooks, *Anal. Chem.*, **75**, 313 (2003).
- M. R. Moghaddam, S. Carrara, and C. F. Hogan, *Chem. Commun.*, **55**, 1024 (2019).
- H. Li, L. Bouffier, S. Arbault, A. Kuhn, C. F. Hogan, and N. Sojic, *Electrochem. Commun.*, **77**, 10 (2017).
- M. Sentic, S. Arbault, L. Bouffier, D. Manojlovic, A. Kuhn, and N. Sojic, *Chem. Sci.*, **6**, 4433 (2015).
- M. Sentic, G. Loget, D. Manojlovic, A. Kuhn, and N. Sojic, *Angew. Chem. Int. Ed.*, **51**, 11284 (2012).
- L. Qi, Y. Xia, W. Qi, W. Gao, F. Wu, and G. Xu, *Anal. Chem.*, **88**, 1123 (2016).
- Q. Zhai, X. Zhang, Y. Han, J. Zhai, J. Li, and E. Wang, *Anal. Chem.*, **88**, 945 (2016).
- S. E. Fosdick, K. N. Knust, K. Scida, and R. M. Crooks, *Angew. Chem. Int. Ed.*, **52**, 10438 (2013).
- G. Loget, D. Zigah, L. Bouffier, N. Sojic, and A. Kuhn, *Acc. Chem. Res.*, **46**, 2513 (2013).
- M. Ongaro, A. Gambirasi, and P. Ugo, *ChemElectroChem*, **3**, 450 (2016).
- M. Li, S. Liu, Y. Jiang, and W. Wang, *Anal. Chem.*, **90**, 6390 (2018).
- M. Hasheminejad, Y. Fang, M. Li, Y. Jiang, W. Wang, and H.-Y. Chen, *Angew. Chem. Int. Ed.*, **56**, 1629 (2017).
- A. L. Dauphin, A. Akkach, S. Voci, A. Kuhn, G. Xu, L. Bouffier, and N. Sojic, *J. Phys. Chem. Lett.*, **10**, 5318 (2019).
- P. A. Defnet and B. Zhang, *ChemElectroChem*, **7**, 252 (2020).
- T. J. Anderson, P. A. Defnet, and B. Zhang, *Anal. Chem.*, **92**, 6748 (2020).
- L. Bouffier, S. Arbault, A. Kuhn, and N. Sojic, *Anal. Bioanal. Chem.*, **408**, 7003 (2016).

43. A. Bouchet, E. Descamps, P. Mailley, T. Livache, F. Chatelain, and V. Haguët, *Small*, **5**, 2297 (2009).
44. X. Zhang, Q. Zhai, H. Xing, J. Li, and E. Wang, *ACS Sens.*, **2**, 320 (2017).
45. W. Zhan, J. Alvarez, and R. M. Crooks, *J. Am. Chem. Soc.*, **124**, 13265 (2002).
46. W. Gao, K. Muzyka, X. Ma, B. Lou, and G. Xu, *Chem. Sci.*, **9**, 3911 (2018).
47. W. Qi, J. Lai, W. Gao, S. Li, S. Hanif, and G. Xu, *Anal. Chem.*, **86**, 8927 (2014).
48. L. Bouffier, D. Zigah, C. Adam, M. Sentic, Z. Fattah, D. Manojlovic, A. Kuhn, and N. Sojic, *ChemElectroChem*, **1**, 95 (2014).
49. M. Sentic, S. Arbault, B. Goudeau, D. Manojlovic, A. Kuhn, L. Bouffier, and N. Sojic, *Chem. Commun.*, **50**, 10202 (2014).
50. X. Zhang, C. Chen, J. Li, L. Zhang, and E. Wang, *Anal. Chem.*, **85**, 5335 (2013).
51. C. Warakulwit, T. Nguyen, J. Majimel, M.-H. Delville, V. Lapeyre, P. Garrigue, V. Ravaine, J. Limtrakul, and A. Kuhn, *Nano Lett.*, **8**, 500 (2008).
52. Y.-L. Ying, R. Gao, Y.-X. Hu, and Y.-T. Long, *Small Meth.*, **2**, 1700390 (2018).
53. R.-J. Yu, Y.-L. Ying, R. Gao, and Y.-T. Long, *Angew. Chem. Int. Ed.*, **58**, 3706 (2019).
54. J. Liu, R. Bombera, L. Leroy, Y. Roupioz, D. R. Baganizi, P. N. Marche, V. Haguët, P. Mailley, and T. Livache, *PLoS One*, **8**, e57717 (2013).
55. J. Liu et al., *Anal. Chem.*, **84**, 3254 (2012).
56. Y.-L. Ying, Y.-X. Hu, R. Gao, R.-J. Yu, Z. Gu, L. P. Lee, and Y.-T. Long, *J. Am. Chem. Soc.*, **140**, 5385 (2018).
57. C. Cao and Y.-T. Long, *Acc. Chem. Res.*, **51**, 331 (2018).
58. R. Gao, Y.-L. Ying, Y.-X. Hu, Y.-J. Li, and Y.-T. Long, *Anal. Chem.*, **89**, 7382 (2017).
59. C. Ma, W. Wu, L. Li, S. Wu, J. Zhang, Z. Chen, and J.-J. Zhu, *Chem. Sci.*, **9**, 6167 (2018).
60. Y. Wang, R. Jin, N. Sojic, D. Jiang, and H.-Y. Chen, *Angew. Chem. Int. Ed.*, **59**, 10416 (2020).
61. A. Ismail et al., *Anal. Chem.*, **91**, 8900 (2019).
62. S. Arya, S. Khan, A. Vaid, H. Kour, and P. Lehana, *J. Nano- Electron. Phys.*, **5**, 01001 (2012).
63. P. Pham, S. Roux, F. Matonti, F. Dupont, V. Agache, and F. Chavane, *J. Neural Eng.*, **10**, 046002 (2013).
64. W. Miao, J.-P. Choi, and A. J. Bard, *J. Am. Chem. Soc.*, **124**, 14478 (2002).
65. A. Zanuti et al., *Nat. Commun.*, **11**, 2668 (2020).
66. G. Valenti, A. Fiorani, H. Li, N. Sojic, and F. Paolucci, *ChemElectroChem*, **3**, 1990 (2016).